Bending martensite needles in $Ni_{65}Al_{35}$ investigated by two-dimensional elasticity and high-resolution transmission electron microscopy

Ph. Boullay and D. Schryvers
EMAT, University of Antwerp, RUCA, Groenenborgerlaan 171, B-2020 Antwerpen, Belgium

R. V. Kohn
Courant Institute of Mathematical Sciences, 251 Mercer Street, New York, New York 10012
(Received 27 March 2001; published 20 September 2001)

The bending and tapering of microtwin needles at the interface between two martensite laminates in $Ni_{65}Al_{35}$ are addressed. A theory is presented, based on the assumption that the microstructure is essentially stress-free; it predicts a linear relationship between the bending and tapering of the needles. The predictions of this theory are compared to experimental data obtained by high-resolution transmission electron microscopy. The agreement between theory and experiment is good, thus bridging the gap between continuum theory and discrete atomic structure, particularly in the region where the bending and tapering are largest.

DOI: 10.1103/PhysRevB.64.144105 PACS number(s): 61.72.Bb, 81.30.Kf, 68.37.Lp, 61.50.Ah

I. INTRODUCTION

The alloy $Ni_{65}Al_{35}$ undergoes a first order cubic-to-tetragonal martensitic transformation upon cooling. The high temperature β-phase ($B2$ austenite) has a CsCl-type unit cell. The low-temperature β phase ($L1_0$ martensite) occurs in three equally probable deformation variants due to the reduction of symmetry. As in many symmetry breaking phase transformations, microstructures form upon cooling at parent-product interfaces, mixing two or more variants of martensite to minimize the stress. Once the cooling is completed the parent phase has disappeared, but the microstructures of the product phase remain. In Ni-Al, these microstructures are typically laminates (plates) mixing two variants of martensite, henceforth referred to as variants 1 and 2. Within each laminate these variants match coherently along so-called microtwin planes parallel to the close packed planes of the product structure.[1,2] Where two laminates with different twin planes meet they form interesting, macroscopically coherent nanostructures: such interfaces may be called ''approximate interfaces'' or ''macrotwin boundaries,'' referring to their width and average mirror nature, respectively.

This paper considers a specific, relatively common type of macrotwin boundaries in Ni-Al martensite. It occurs when both laminates are made from the same two variants, which results in a macrotwin boundary macroscopically parallel to a former $\{100\}_\beta$ type plane. As we shall explain presently, the microstructural character of the boundary can take two different forms ''crossings'' or ''steps,'' depending on the local environment. This paper addresses the details of the second case, namely, steps, whereas the crossings will be treated in a forthcoming paper. Each step is essentially parallel to a microtwin plane and along the step the microtwins are nearly unperturbed on one side, while they bend and taper into needles on the other. Further discussion of this macrotwin boundary and how it arises—including discussion of the underlying phase transformation, and the details of the experiments—can be found in Refs. 3–5. Such bending and tapering is observed in conventionally treated bulk material[2] as well as in splat-cooled samples.[6] Equivalent structures are also seen in other materials, including the shape-memory alloy CuAlNi.[7]

In the present paper a theory is presented, based on the assumption that the final microstructure is essentially stress-free; it uses linear elasticity, drawing in part on prior work,[8] and it predicts a linear relationship between the bending and tapering of the needles. The predictions of this theory are compared with atomic-scale measurements, obtained by analyzing experimental high-resolution transmission electron microscopy (HRTEM) images. The experiments and theory are in good agreement, particularly in the region where the bending and tapering are largest. The present fit between theoretical calculations performed in a continuum framework and experimental values directly obtained from images revealing the discrete nature of the atomic lattice could proof to be an important step in bridging the gap between distinctive dimensional scales.

II. EXPERIMENTAL OBSERVATIONS

Figure 1(a) shows a typical transmission electron microscopy (TEM) image of the macrotwin boundary between two martensite laminates. Each laminate is composed of the same two variants of martensite, visible in the image as bright and dark bands as a result of the bright field imaging condition and a slight tilt of the sample away from a perfect zone orientation with edge-on microtwin planes. The planar interfaces between two adjacent variants are the close packed and essentially stress-free microtwin planes at which the two variants meet coherently. For the present material, the amount of lattice distortion yields an average volume fraction close to 1/3.[2,9–11] From corresponding diffraction patterns and HRTEM images it is clear that the widest variants on both sides belong to the same type, which we will choose to be variant 1.

The complexity of the microstructure near the macrotwin boundary arises from mismatching rotations. Indeed, the orientation of the lattices of variant 1 is not identical in the two laminates; rather, they differ by a rotation of about 7°. The same applies of course to the variant 2 microtwins, but with a different value of $-14°$ due to the rigid body rotations of

 ©2001 The American Physical Society

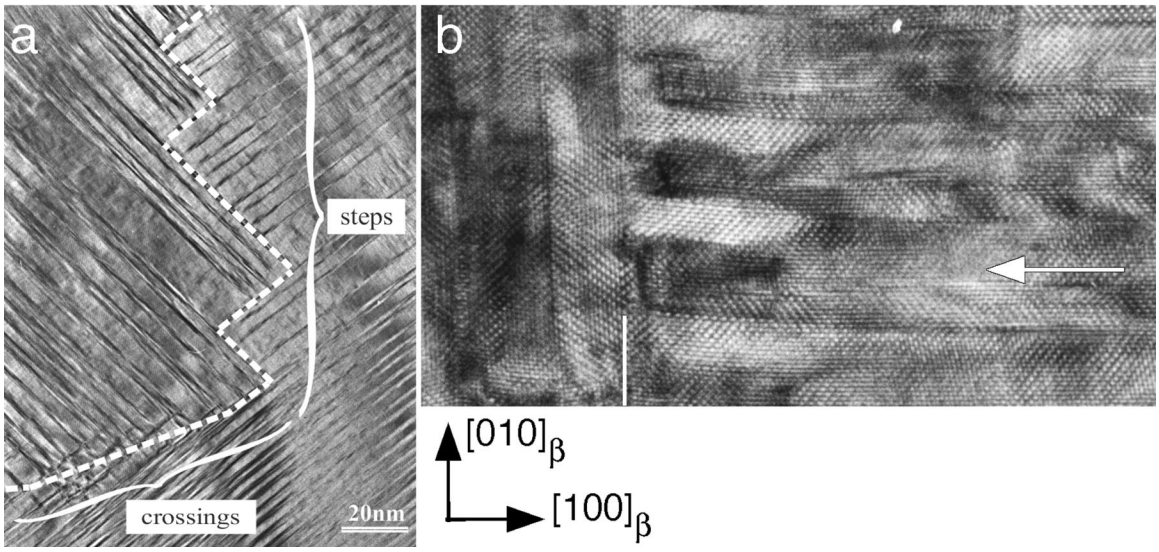

FIG. 1. (a) Typical TEM image of a macrotwin boundary in $Ni_{65}Al_{35}$ martensite revealing crossing and step type microstructures. (b) HRTEM enlargement of a step revealing the atomic lattice bending when looking along the arrow. The indicated lattice directions at the bottom refer to the orientation of the original β austenite corresponding with (a).

both laminates already existing before the macrotwin boundary is formed.[3,5] So the variants cannot simply heal across the approximate interface; they must do something more complex, to accommodate the change in rotation.

Upon examination of Fig. 1(a) it is seen that there are two essentially different local microstructures, labeled ''crossings'' and ''steps.'' The steps are locally parallel to alternating $\{110\}_\beta$ and $\{1\bar{1}0\}_\beta$ planes, only on average leading to the preferred $\{100\}_\beta$ orientation for the microtwin plane at a larger scale. The part labeled ''crossings'' is actually only a small portion of the present interface, but it can be distinguished by the fact that the microtwins from both laminates penetrate into the other one, whereas at a step several microtwins of one laminate are seen to stop at one microtwin plane of the other laminate. In cases where the crossings extend over a large region, the central macrotwin plane is immediately parallel with a $\{100\}_\beta$ plane. Examples of the latter are presented and discussed elsewhere.[3–5] In general it is found that a crossing type is preferred when the local volume fractions on both sides are constant and stable.[3,4] On the other hand, if, for whatever reason, the local volume fraction on one side differs strongly from the average value, a step type is observed.

This paper focusses on the step-type interface. At the scale of a single step, the local orientation of the approximate interface is a microtwin plane. On one side the microstructure is simply twinned, ending with the smallest variant 2. On the other side the variant 2 twins taper into needles, leaving only variant 1 at the macrotwin boundary as seen in the enlargement of Fig. 1(b). In the latter image the geometry of the white dot pattern reflects the tetragonality of the martensite lattice, for which the c/a ratio can thus immediately be measured. As the microtwins taper, these twins also bend, and the resulting rotation changes the orientation of the lattice in the retained variant 1 to match that of the other laminate. Our goal is a quantitative analysis of this tapering and bending.

The region near the approximate interface is certainly stressed, as is seen in Fig. 1(b) from the strong changes in image contrast on a scale of a few nm, and there can be dislocations as well. We believe, however, that incoherence and stress play a relatively minor role, and our theory is founded on this viewpoint. This is supported by the fact that the atomic lattice remains resolved in nearly the entire HRTEM image, even close to the interface, indicating that the atomic columns remain undistorted along the viewing or z direction.

In what follows the proposed theoretical description is presented first, indicating the relevant parameters to be measured from the experimental images. Then these data are obtained for a number of different examples and compared with the theoretical model.

III. THEORETICAL ANALYSIS OF THE BENDING DEFORMATION

The microstructures under consideration mix just two variants of martensite. Their transformation strains relative to the cubic parent β phase are $U_1 = \mathrm{diag}(\eta_3, \eta_1, \eta_1)$ and $U_2 = \mathrm{diag}(\eta_1, \eta_3, \eta_1)$ and the twins planes are $(110)_\beta$ and $(1\bar{1}0)_\beta$. It is convenient, however, to work in a different coordinate system, rotated by $\pi/4$ about the z axis (i.e., the viewing direction of the TEM images), so that the twin planes are coordinate planes. In this rotated coordinate system the transformation strains are

$$U_1 = \begin{pmatrix} \frac{\eta_1+\eta_3}{2} & \frac{\eta_1-\eta_3}{2} & 0 \\ \frac{\eta_1-\eta_3}{2} & \frac{\eta_1+\eta_3}{2} & 0 \\ 0 & 0 & \eta_1 \end{pmatrix},$$

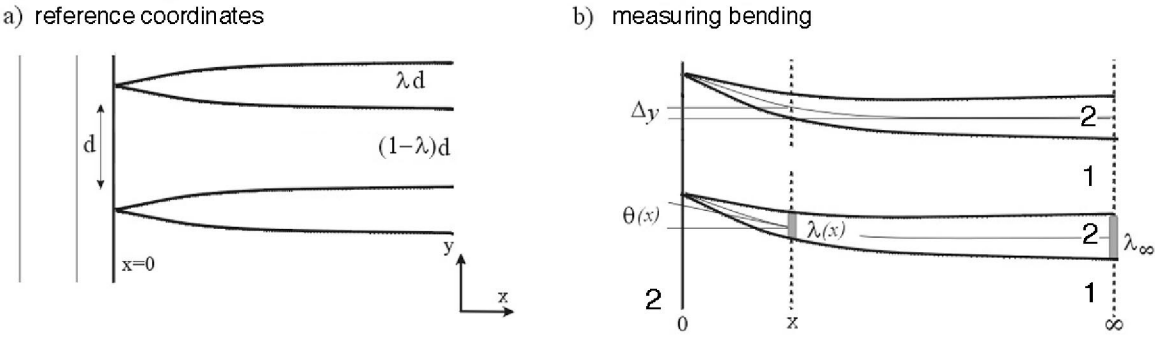

FIG. 2. Reference positions and notations used for the description of bending and tapering in the needle patterns, including the definition of the bending parameters as well as the variant numbers.

$$U_2=\begin{pmatrix} \frac{\eta_1+\eta_3}{2} & \frac{\eta_3-\eta_1}{2} & 0 \\ \frac{\eta_3-\eta_1}{2} & \frac{\eta_1+\eta_3}{2} & 0 \\ 0 & 0 & \eta_1 \end{pmatrix}.$$

In the framework of geometrically linear elasticity, it is convenient to write these as

$$U_1=I+\begin{pmatrix} \varepsilon_1 & \delta & 0 \\ \delta & \varepsilon_1 & 0 \\ 0 & 0 & \varepsilon_2 \end{pmatrix}, \quad U_2=I+\begin{pmatrix} \varepsilon_1 & -\delta & 0 \\ -\delta & \varepsilon_1 & 0 \\ 0 & 0 & \varepsilon_2 \end{pmatrix},$$

where $\varepsilon_1=(\eta_1+\eta_3)/2-1$, $\varepsilon_2=\eta_1-1$ and $\delta=(\eta_1-\eta_3)/2$.

Figure 2 shows schematically the structure that will be analyzed. The local approximate interface is the plane $x=0$ in reference coordinates of the austenite. To its left is a region of twinned martensite, with twin planes parallel to the (y,z) plane, ending at $x=0$ with variant 2. To its right is a different region of twinned martensite, with twin planes parallel to the (x,z) plane. Far from the approximate interface the twins on the right are uniform. Near the approximate interface, however, the twins of variant 2 taper into needles, so that at $x=0$ only variant 1 is present. The volume fraction λ of the needle variant 2 is thus a function of x, with $\lambda(0)=0$ and $\lambda(x)\to\lambda_\infty$ as $x\to\infty$. In the reference coordinates the shapes that will become the needles after the transformation are symmetric, as shown in Fig. 2(a). Deformation during the transformation breaks the symmetry, making them bend as they approach the approximate interface, as shown in Fig. 2(b) [see also Fig. 1(b)].

The schematic in Fig. 2 is periodic in y. The present theoretical approach does not require strict periodicity, but macroscopic homogeneity in the y direction is assumed. This permits the averaging of various quantities (e.g., volume fraction or strain) with respect to y. For any function $f(x,y)$, one can write $\overline{f}(x)=$average of f with respect to y.

Neglecting dislocations, the present microstructure can be viewed as a mixture of two coherent elastic phases, i.e., the two martensite variants 1 and 2.[10] Within the framework of linear elasticity, it is natural to assume that the map from reference to deformed position has the form

$$(x,y,z)\mapsto[x+\varepsilon_1 x+u(x,y),y+\varepsilon_1 y+v(x,y),z+\varepsilon_2 z] \tag{1}$$

since the associated linear strain is

$$\begin{pmatrix} \varepsilon_1+u_x & \frac{u_y+v_x}{2} & 0 \\ \frac{u_y+v_x}{2} & \varepsilon_1+v_y & 0 \\ 0 & 0 & \varepsilon_2 \end{pmatrix}$$

with u_x the partial derivative of u by x, etc. The ansatz (1) reduces the problem to one of 2D linear elasticity, involving a displacement $[u(x,y),v(x,y)]$ whose linear strain

$$e(x,y)=\begin{pmatrix} u_x & \frac{u_y+v_x}{2} \\ \frac{u_y+v_x}{2} & v_y \end{pmatrix}$$

prefers eigenstrains e_1 in variant 1 and e_2 in variant 2, where

$$e_1=\begin{pmatrix} 0 & \delta \\ \delta & 0 \end{pmatrix}, \quad e_2=\begin{pmatrix} 0 & -\delta \\ -\delta & 0 \end{pmatrix}. \tag{2}$$

This 2D, two-phase problem was studied in Ref. 8 where elastic energy minimization was used to simulate the microstructure. The viewpoint of the present paper, however, is somewhat different from that of Ref. 8. Here, we do not attempt to predict the shapes of the needles. Rather, these shapes are treated as data to be determined experimentally by measuring $\lambda(x)$, the volume fraction of the needles at distance x from the approximate interface. A simple, kinematic relation linking the bending of the needles to their tapering will be derived. The theoretical 2D approach is supported by the fact that the HRTEM images taken along the z direction still reveal a well-resolved lattice indicating no or very little lattice distortions along the atomic columns.

The present analysis is founded on a few basic principles, which are now stated and their origin explained. Principle 1. In the uniformly twinned region far from the approximate interface, i.e., as $x\to\infty$

$$u_x=0, \quad u_y=\pm 2\delta, \quad v_x=v_y=0. \tag{3}$$

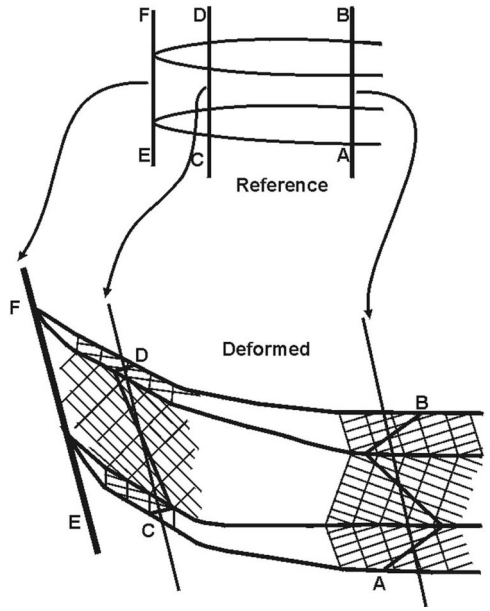

FIG. 3. Microstructural interpretation of principle 2: the $x=$ constant lines AB, CD, and EF remain macroscopically parallel with one another after deformation.

Indeed, the uniformly twinned structure is exactly stress-free, so $e(x,y)$ takes exactly the values e_1 and e_2. This determines u and v up to an infinitesimal rigid motion. A convenient choice of this rigid motion gives Eq. (3).

Principle 2. The planes $x=$constant remain macroscopically parallel after deformation, i.e.,

$$\overline{u_y} \text{ is independent of } x. \tag{4}$$

This follows from the form of the eigenstrains. Indeed, since both variants prefer $u_x=0$, we expect u_x to be negligible throughout the microstructure. So for any $0<x_1<x_2$ and any y,

$$u(x_2,y)-u(x_1,y)=\int_{x_1}^{x_2} u_x(x,y)\,dx \approx 0.$$

Differentiating in y and then integrating (averaging) over y, we conclude that

$$\overline{u_y}(x_2)-\overline{u_y}(x_1)\approx 0.$$

This gives Eq. (4), up to small corrections due to deviation of u_x from its stress-free value of 0. Translating this into the actual microstructure and atomic lattice deformations yields Fig. 3. The lines AB, CD, and EF (i.e., $x=$const) are parallel and straight in the reference austenite lattice. The image of EF in the deformed (physical) variables is also straight—this is the step. The images of AB and CD are, however, not straight; rather, they oscillate around macroscopic lines with a well-defined slope. Principle 2 tells us that these lines are parallel to the step, as shown in Fig. 3.

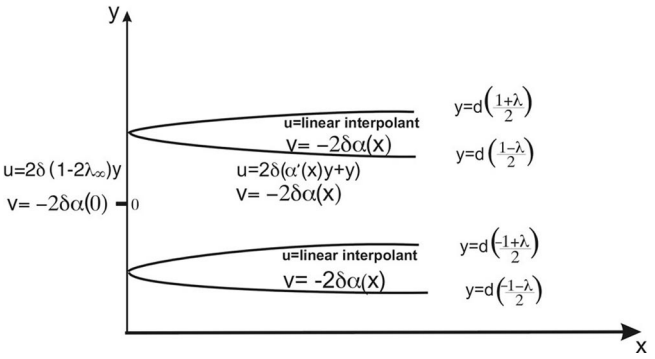

FIG. 4. Example of a deformation satisfying principles 1–3 (Ref. 8) with $u(x,y+d)=u(x,y)+2\delta(1-2\lambda_\infty)d$ and $\alpha'(x)=2[\lambda(x)-\lambda_\infty]$.

Notice that principles 1 and 2 determine the value of u_y uniquely:

$$\overline{u_y}=2\delta(1-\lambda_\infty)+(-2\delta)\lambda_\infty=2\delta(1-2\lambda_\infty), \tag{5}$$

where λ_∞ is the volume fraction of the needles (variant 2) far from the approximate interface.

Principle 3. The shear strain e_{12} takes values $\pm\delta$, i.e.,

$$\frac{u_y+v_x}{2}=\begin{cases} -\delta & \text{inside the needles,} \\ \delta & \text{outside the needles,} \end{cases} \tag{6}$$

for all $x>0$. This follows again from the form of the eigenstrains, which prefer $e_{12}=\delta$ in variant 1 (outside the needles) and $e_{12}=-\delta$ in variant 2 (inside the needles). As we expect the microstructure to be approximately stress-free, Eq. (6) holds, up to small corrections due to deviation of e_{12} from its stress-free values.

One might wonder whether these principles are consistent, and what sort of deformation they permit. Figure 4 answers these questions by providing an example of an elastic displacement consistent with our principles. The horizontal component u is periodic in y with $u(x,y+d)=u(x,y)+2\delta(1-2\lambda_\infty)d$, so it has $\overline{u_y}=2\delta(1-2\lambda_\infty)$, consistent with principles 1 and 2. The vertical component is $v=-2\delta\alpha(x)$, independent of y. Outside the needles the example consists of pure bending plus a uniform shear; inside the needles u is determined by linear interpolation in y. Therefore we have, along any line $x=x_0$

$$u_y=\begin{cases} \dfrac{1}{\lambda}\overline{u_y}-\dfrac{1-\lambda}{\lambda}2\delta(\alpha'+1) & \text{inside the needles (fraction } \lambda), \\ 2\delta(\alpha'+1) & \text{outside the needles [fraction } (1-\lambda)] \end{cases}$$

from which it follows that

$$u_y + v_x = \begin{cases} 2\delta[(\lambda - 2\lambda_\infty - \alpha')/\lambda] & \text{inside the needles,} \\ 2\delta & \text{outside the needles.} \end{cases}$$

Therefore the example satisfies principle 3 as well, if $\alpha'(x) = 2[\lambda(x) - \lambda_\infty]$.

We claim that, for any deformation satisfying principles 1–3, the observed bending angle $\theta(x)$ at distance x from the approximate interface satisfies

$$\tan\theta(x) = 4\frac{|\eta_1 - \eta_3|}{\eta_1 + \eta_3}[\lambda_\infty - \lambda(x)]. \tag{7}$$

[See Fig. 2(b) for the definitions of $\theta(x)$, $\lambda(x)$, and λ_∞.] Indeed, as noted above, principles 1 and 2 give

$$\overline{u_y} = 2\delta(1 - 2\lambda_\infty).$$

However, principle 3 gives

$$\begin{aligned} \overline{u_y + v_x} &= 2\delta[1 - \lambda(x)] + (-2\delta)[\lambda(x)] \\ &= 2\delta[1 - 2\lambda(x)] \quad \text{for any } x > 0 \end{aligned}$$

so it is concluded that

$$\overline{v_x} = 4\delta[\lambda_\infty - \lambda(x)]. \tag{8}$$

Under the ansatz (1) the deformed midline of a needle is the image of

$$x \mapsto [x + \varepsilon_1 x + u(x, y_0), \quad y_0 + \varepsilon_1 y_0 + v(x, y_0), \quad z_0 + \varepsilon_2 z_0],$$

so its slope is

$$-\tan(\theta) = \frac{v_x}{1 + \varepsilon_1 + u_x}. \tag{9}$$

Since the microstructure is nearly stress-free, both u_x and v_y are negligible (see the discussion of principle 2). Therefore we may ignore the contribution of u_x on the right-hand side of Eq. (9), and we may replace v_x by $\overline{v_x}$. Taking absolute values, this gives

$$\tan\theta(x) = \frac{|\overline{v_x}|}{(1 + \varepsilon_1)} = \frac{4|\delta|}{(1 + \varepsilon_1)}[\lambda_\infty - \lambda(x)], \tag{10}$$

which is precisely relation (7).

The preceding analysis determines the direction of the bending as well as its magnitude. The present Ni-Al material has $\delta = (\eta_1 - \eta_3)/2 < 0$, so Eq. (8) gives $v_x < 0$, consistent with Fig. 2(b). If the needles contained variant 1 rather than variant 2 then they would bend the other way. Indeed, this case is obtained by replacing δ by $-\delta$ in the formulas given above, which changes the sign of v_x. In this case variant 2 would be retained at the approximate interface which has indeed to be rotated in opposite sense in order to match the variant 2 orientation to the left of the boundary. Note that if the needles contain variant 1 then the layer just to the left of the approximate interface must also contain variant 1.

Our analysis shows that the amount of bending is proportional to λ_∞. Thus the bending should be most pronounced when the volume fraction of the needle variant is large ($\lambda_\infty \approx 1$). This effect cannot easily be observed in Ni-Al alloys, because the value of λ_∞ is always around 1/3.[2] However, the effect of varying λ_∞ is very clear in the work of Abeyaratne, Chu and James on CuAlNi,[7] where similar two-phase microstructures are observed and the volume fraction is varied by applying stress.

IV. COMPARISON OF THEORY WITH EXPERIMENT

From the theoretical treatment it is clear that the bending is expected to be related to the tapering, which can be measured through the changing volume fraction. The common parameter here is the distance into the plate accommodating the bending variants and measured from the atomic plane separating the bending variants from the unaffected plate. The values δ and ε_1, which depend on the deformation parameters and thus are constant for a given composition, have to be measured. In what follows different approaches for obtaining these parameters from the experimental images are discussed.

A. Determining δ and ε_1

The parameters $\delta = (\eta_1 - \eta_3)/2$ and $\varepsilon_1 = (\eta_1 + \eta_3)/2 - 1$ can be obtained by measuring the elongation η_3 of the cubic c direction and the compression η_1 of the a and b directions during the martensitic transformation. This should in principle be performed by measuring the lattice parameters of the austenite as well as the martensite at the transformation temperature (approximately 400 °C). However, the present HRTEM work is based on the study of materials which are completely transformed into martensite, which means that one can not access the cell parameter of the austenitic state. Thus, as the exact δ and ε_1 values for our material are unknown, a first option is to use values available from the literature on Ni-Al material, possibly with a slightly different composition. Alternatively, as the Ni-Al martensitic transformation implies shape memory behavior, one can assume volume preservation[12,13] during the transformation which enables one to obtain η_1 and η_3 only from the martensite lattice. To begin with, three sets of values, obtained from different sources and under different assumptions, are suggested.

(1) $\eta_3 = 1.083$ and $\eta_1 = 0.939$ from $Ni_{62.5}Al_{37.5}$ melt-spun samples measured by electron microscopy as both austenite and martensite coexist for this composition.[14] This gives a first set of values of $\delta_1 = -0.072$ and $\varepsilon_{11} = 0.011$.

(2) $\eta_3 = 1.1302$ and $\eta_1 = 0.9392$ for $Ni_{66}Al_{34}$ bulk material and obtained by combining x-ray diffraction[15] and HRTEM.[2] This gives a second set of values of $\delta_2 = -0.0955$ and $\varepsilon_{12} = 0.0347$.

(3) $\eta_3 = 1.15$ and $\eta_1 = 0.93$ from the present $[110]_\theta$ HRTEM images assuming volume preservation. This gives a third set of values of $\delta_3 = -0.11$ and $\varepsilon_{13} = 0.04$.

As the δ an ε_1 values from the $Ni_{62.5}Al_{37.5}$ compound differ quite strongly from those for the $Ni_{66}Al_{34}$ and those

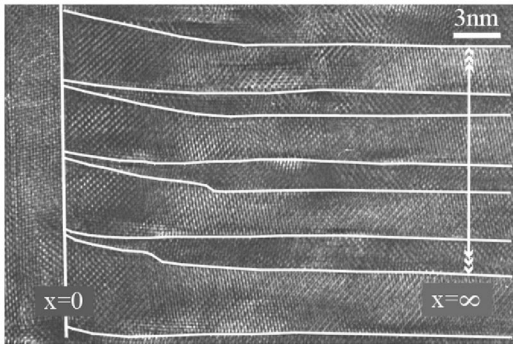

FIG. 5. Typical HRTEM image of a nanoscale martensite needle pattern. The microtwin boundaries are emphasized as well as a typical length for measuring the volume fraction

assuming volume preservation in the present material, only the second and third suggestions will be retained.

B. Measuring λ_∞ and $\lambda(x)$

The parameters λ_∞ and $\lambda(x)$ can easily be obtained from a TEM image by measuring the relative widths of the microtwin variants at a given value for x. Attention should be paid to measure λ for the local area under investigation: only four to a maximum of eight microtwin variants are typically present at a single step region [see Fig. 1(a)]. The transition layer in which the bending occurs is typically of the order of 10 nm wide measured along the x axis (see Fig. 5). Consequently, the parameters λ_∞ and $\lambda(x)$ can be obtained from a single HRTEM image. The measure of λ is made manually with a ruler on an enlarged HRTEM picture. The major uncertainty on the measures comes from the choice of the envelope of the needles since its limits are not necessarily obvious in the picture especially when getting closer to the interface, i.e., for the tips of the needles.

C. Comparing theory with experiment

The values for $\theta(x)$ cannot directly be measured from the HRTEM pictures and the following procedure is used. In order to be able to easily follow the bending, the traces of the $(110)_\beta$ or $(1\bar{1}1)_\theta$ planes (i.e., the microtwin planes) are enhanced by Fourier filtering. Then the filtered image is superimposed onto the original HRTEM image, as shown in Fig. 6, which provides a reference for distances as the cell parameters of the martensite are known.

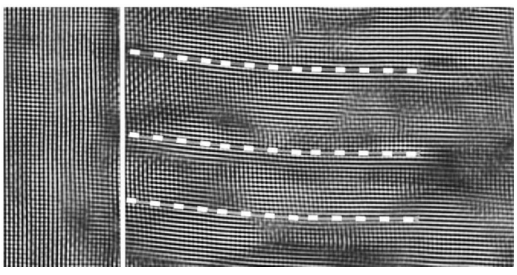

FIG. 6. Superposition of an original and a filtered HRTEM picture. The three planes taken to measure the bending deformation are indicated by dashed lines

As indicated in Fig. 2(b), for a given x, the indicative parameter of the bending is the value Δy which measures the displacement in the y direction of a lattice point from the reference plane. When the function $\Delta y = f_\Delta(x)$ is experimentally measured, it can be compared to the theory by numerically integrating the proposed expression for $d\Delta y/dx = -\tan\theta(x)$ given in Eq. (7). As the experimental measures are always performed in the deformed system, the coordinates used when measuring HRTEM images are actually $x(1+\varepsilon_1)$ and $y(1+\varepsilon_1)$ when compared with the reference (x,y) coordinates used in the theory. As the final comparison is that of $\tan\theta(x)$, this, however, has no impact on the final numerical results.

To measure the bending deformation for a given step in practice, typically three traces of $(1\bar{1}1)_\theta$ planes are chosen as indicated in Fig. 6. For each trace, $\Delta y = f_\Delta(x)$ is measured followed by averaging per x position. The calculation of the function $\tan\theta(x)$ given in the theoritical relation is performed from the experimental measure of $\lambda(x)$. The theoretical estimate of the function $\Delta y = f_\Delta(x)$ is then obtained by numerical integration (cumulative sum) of $\tan\theta(x)$. The values $\Delta y = f_\Delta(x)$ found from this calculation can then be compared directly with the observed ones.

V. DISCUSSION

In the example of Fig. 5, the bending of the three traces of the $(1\bar{1}1)_\theta$ planes is very similar. In another case, taken from the same sample, the presence of dislocations disturbs the continuous bending of the traces of the $(1\bar{1}1)_\theta$ planes, which illustrates the experimental difficulty to estimate an average bending deformation for a given area. This also illustrates the fact that the bending deformation can be different from one area to the other. When limiting our measurements to situations where no dislocations are observed, a full treatment of the experimental measures yields the plots shown in Fig. 7. Here both the x dependence of Δy and λ are presented. It is important to note that both factors indeed start to change at the same distance from the reference plane at $x=0$. The major influence on the precision of the measurements is that of the averaging over different planes or variants.

In Fig. 8 the latter results are compared with the calculation as explained above and using both suggested values for δ and ε_1. The uncertainty on the input values for δ, ε_1, and λ are incorporated into the theoretical curves, yielding the uncertainty flags around the calculated points. It can be seen that the correlation between the start of the bending and tapering is very well reproduced. Changing the values of δ and ε_1 yields a slightly different curvature, with the best match found for the deformation parameters δ and ε_1 obtained from the present HRTEM images assuming volume preservation. Still, the curvature of the experimental graph when approaching the interface is stronger than that of the two cases of the theoretical approach, even when including the uncertainty flags. When data is collected from an image in which the bending is accompanied by dislocations, the experimental graph tends to have a slower curve.

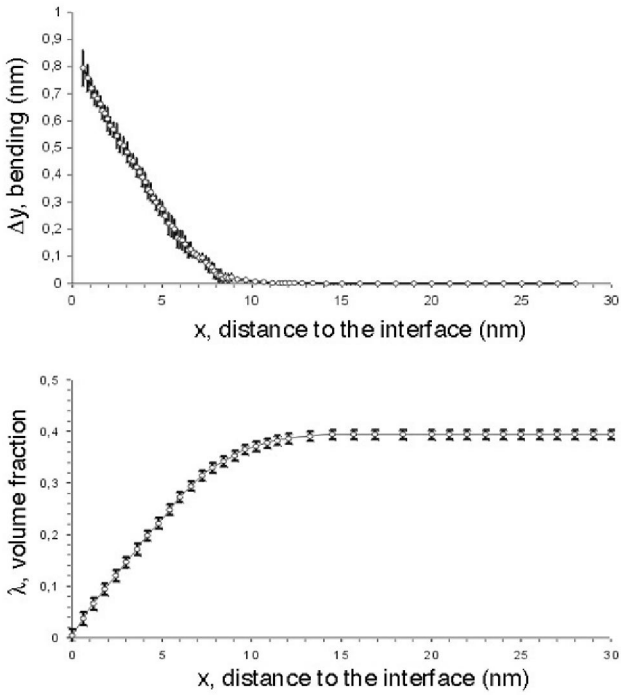

FIG. 7. Experimental measures of (a) the bending and (b) tapering as obtained by averaging over several planes and variants, respectively.

It should be noted that the present theory successfully captures the link between bending and tapering in the region where both effects are large, i.e., for x below about 5 nm. Indeed, our main conclusion is that

$$\frac{d\Delta y}{dx} = 4\frac{\eta_1 - \eta_3}{\eta_1 + \eta_3}[\lambda_\infty - \lambda(x)].$$

The experiments bear this out, even quantitatively, in the region very near the approximate interface where the slopes of all curves are indeed the same. The theory is less successful in the region around 5–10 nm from the approximate interface, where the bending and tapering are small. The curvature in the $(x,\Delta y)$ graph is clearly larger in this region than our theory would suggest.

It is not surprising that our theory does best where the tapering and bending are largest. Indeed, our analysis ignores any role of incoherence or stress, but there is of course some stress, and often some incoherence. Where the geometrical effects (tapering and bending) are large, the impact of stress and incoherence is truly secondary. But where the geometrical effects are smallest the roles of stress and incoherence are naturally more significant. It is not clear at present whether a more extensive theory as that of finite elasticity[11] would solve this discrepancy, as the latter occurs far from the approximate interface where the loss of accuracy due to linearization would seem to be smallest. Still it should be remarked that the atomic scale bending and measures from images of a discrete lattice are relatively well described in the framework of a continuum theory, which opens potential ways for bridging the gap between those essentially different concepts and dimensionality scales.

In relation with the overall nanostructures and microstructures observed around these type of macrotwin boundaries, i.e., those with the same combination of martensite variants with the same volume ratio on both sides, it should be mentioned that the present bending and tapering is only one of the possible structural features the system uses to accommodate remaining stresses when two laminates meet. Other means include very small regions ($\leqslant$ 5 nm diameter) at the interface with a slightly different lattice deformation and atomic ledges displacing the microtwin planes from one close packed plane to the next (in the range between 50 and 500 nm away from the interface).[3–5] Although the steps in-

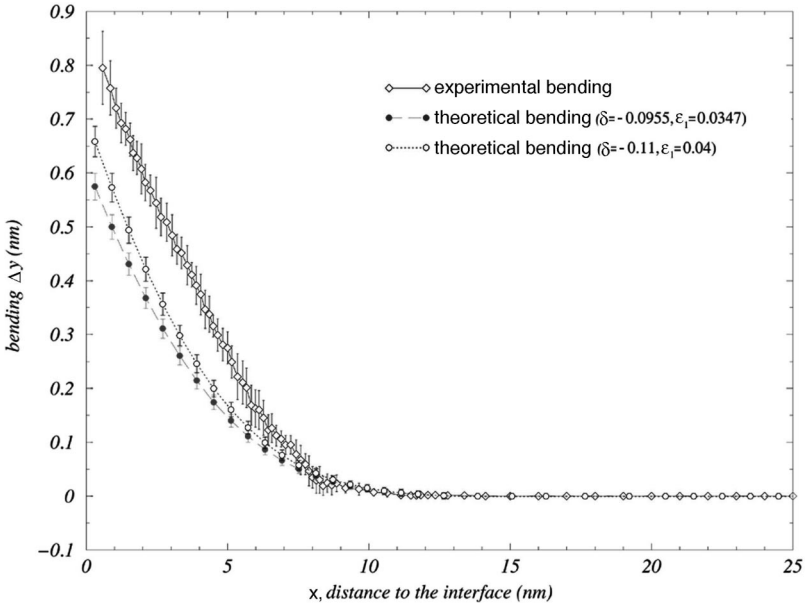

FIG. 8. Comparison of the bending deformation as obtained from experimental data and theoretical prediction. Very near the approximate interface (0–5 nm) the slopes of all curves are the same. The curvature of the experimental graph is clearly larger than the theory suggests in the region around 5–10 nm from the approximate interface, i.e., where the bending and tapering are small.

vestigated here seem to be related with an unstable volume fraction on one side of the interface, the underlying reason for this remains unclear for now.

VI. CONCLUSIONS

The relation between bending and tapering of martensite needles at a macrotwin boundary in $Ni_{65}Al_{35}$ is investigated both from theoretical as well as experimental point of view. The theoretical approach is based on the assumption that the microstructure is essentially stress-free and uses linear elasticity. It predicts a linear relationship between the bending and tapering of the needles, the latter expressed as a function of the volume fraction of the small needle variants. The deformation parameters of the austenite-martensite transformation appear as constants in the obtained expression. The predictions of this theory are compared with atomic-scale measurements, obtained by analyzing experimental high-resolution transmission electron microscopy images. Although the numerical curves obtained from the theoretical predictions and experimental observations fall outside the respective precision ranges, the general trends of the observations are well reproduced by the theory, particularly in the region where the bending and tapering are largest. This can be understood by noting that in this region the assumptions of the theory are indeed best met.

ACKNOWLEDGMENTS

Part of this work was supported by the Trade and Mobility Research program of the EEC under the Project No. FMRX-CT98-0229 within the network entitled ''Phase Transitions in Crystalline Solids.'' Additional support was provided by the U.S. National Science Foundation, and the Isaac Newton Institute at Cambridge University.

[1] S. Chakravorty and C. M. Wayman, Metall. Trans. A **7**, 555 (1976).
[2] D. Schryvers, Philos. Mag. A **68**, 1017 (1993).
[3] Ph. Boullay, D. Schryvers, and J. Ball (unpublished).
[4] D. Schryvers, P. Boullay, R. Kohn, and J. Ball, Proceedings of ESOMAT 2000 [J. de Physique (to be published)].
[5] D. Schryvers, P. Boullay, P. Potapov, and C. Satto, Adv. Solid State Phys. **40**, 375 (2000).
[6] D. Schryvers and D. Holland-Moritz, Intermetallics **5**, 427 (1998).
[7] R. Abeyaratne, C. Chu, and R. D. James, Philos. Mag. **73**, 457 (1996).
[8] R. D. James, R. V. Kohn, and T. W. Shield, J. Phys. IV **5**, 253 (1995).
[9] S. Chakravorty and C. M. Wayman, Metall. Trans. A **7**, 569 (1976).
[10] A. G. Khatchaturyan, *Theory of Structural Transformations in Solids* (John Wiley & Sons, New York, 1983).
[11] J. M. Ball and R. D. James, Arch. Ration. Mech. Anal. **100**, 13 (1987).
[12] K. Bhattacharya, Acta Metall. Mater. **39**, 2431 (1991).
[13] K. Bhattacharya, Arch. Ration. Mech. Anal. **120**, 201 (1992).
[14] P. L. Potapov, P. Ochin, J. Pons, and D. Schryvers, Acta Mater. **48**, 3833 (2000).
[15] S. Ochiai, O. Noguchi, and M. Ueno, J. Jpn. Inst. Met. **51**, 686 (1987).